PHYSICAL REVIEW B **96**, 075445 (2017)

Magnetic states of linear defects in graphene monolayers: Effects of strain and interaction

Simone S. Alexandre and R. W. Nunes[*]
Universidade Federal de Minas Gerais, CP 702, 30123-970, Belo Horizonte, MG, Brazil

(Received 15 February 2017; revised manuscript received 7 July 2017; published 31 August 2017)

The combined effects of defect-defect interaction and strains of up to 10% on the onset of magnetic states in the quasi-one-dimensional electronic states generated by the so-called 558 linear defect in graphene monolayers are investigated by means of *ab initio* calculations. Results are analyzed on the basis of the heuristics of the Stoner criterion. We find that conditions for the emergence of magnetic states on the 558 defect can be tuned by uniaxial tensile parallel strains (along the defect direction) as well as by uniaxial compressive perpendicular strains, at both limits of isolated and interacting 558 defects. Parallel tensile strains and perpendicular compressive strains are shown to give rise to two cooperative effects that favor the emergence of itinerant magnetism on the 558 defect in graphene: enhancement of the density of states (DOS) of the resonant defect states in the region of the Fermi level and tuning of the Fermi level to the maximum of the related DOS peak. On the other hand, parallel compressive strains and perpendicular tensile strains are shown to be detrimental to the development of magnetic states in the 558 defect, because in these cases the Fermi level is found to shift away from the maximum of the DOS of the defect states. Effects of isotropic and unisotropic biaxial strains are also analyzed in terms of the conditions encoded in the Stoner criterion.

DOI: 10.1103/PhysRevB.96.075445

I. INTRODUCTION

Technological applications of two-dimensional (2D) nanomaterials require the ability to control their mechanical, electronic, and magnetic properties. In the last decade, graphene in the 2D monolayer form has become an important subject of research, motivated by its mechanical strength and the rich electronic phenomenology connected with the Dirac-fermion nature of its electronic structure on a scale of ∼1eV around the Fermi level [1–3]. The origin of magnetism in graphene is still debated, being usually associated with the presence of vacancies or adsorbates that tend to bind to vacancies [4–8]. In bypartite lattices, vacancies lead to an imbalance in the electronic occupation of the two sublattices, which leads to stabilization of magnetic ground states, as predicted by the Lieb theorem [9]. In a 2D material such as graphene, vacancies and topological point defects can be created in nonequilibrium densities by electron-beam irradiation [10]. However, full control over such magnetic states is hampered by the random placement of vacancies.

Judicious introduction of structural defects presents an alternative for manipulating the electronic and magnetic properties in 2D materials [1,11–20]. Besides the tilt GBs that inevitably occur in polycrystalline graphene [21–25], a so-called 558 extended line defect was shown to occur in graphene layers grown on Ni substrates [13] as the interface across which the stacking of the graphene layer with respect to the Ni substrate shifts from AB to AC (in the usual convention for layer stacking in close-packed lattices). Furthermore, recent experimental work has introduced a protocol for the formation of this 558 extended defect in a controllable fashion in a graphene monolayer [26], which shows that the possibility of manipulating the electronic and magnetic properties of graphene and other two-dimensional materials, by controllable introduction of defects, is a realistic prospect for the near future.

The morphology of the 558 extended defect, shown in Fig. 1, consists of a periodic unit composed of two side-sharing pentagonal rings connected to an octagonal ring. Alexandre *et al.* [11] employed *ab initio* calculations to show the development of itinerant ferromagnetism in the quasi-one-dimensional (q1D) electronic states that are strongly localized on the core of the 558 defect. The ferromagnetic state obtained by Alexandre *et al.* requires n-type doping in order for the Stoner criterion for a magnetic instability to be met [27,28]. Electron doping shifts the Fermi level to the maximum of a pronounced peak in the electronic density of states (DOS) generated by the extended van Hove singularities that appear at and near the Fermi level, which are characteristic of the q1D electronic states of the 558 extended defect [11] in graphene. Given the similar flat-band mechanism and a spin density that is strongly concentrated on one sublattice of the graphene layer, the magnetic state of the 558 defect is of the same nature as that found on zigzag edges of graphene ribbons, as pointed out in Ref. [11].

The extended van Hove singularities, i.e., the broad flat portions of the defect-related electronic states crossing the Fermi level, signal a strong localization of the q1D defect states that leads to an enhancement of exchange and correlation effects. Tuning the Fermi level to the region of the maximum of the related DOS peak leads to the onset of the magnetic states. Large periodic supercells were employed in Ref. [11], with negligible couplings between the 558 defect in the unit cell and its periodic images, meaning that conditions for the emergence of the magnetic state apply to the case of an isolated and unstrained 558 defect in that study. One is naturally led to consider the formation of magnetic states in the 558 defect in graphene under less restrictive conditions.

Two-dimensional materials grown on mismatched substrates are commonly subject to strain. Moreover, strain engineering opens up the possibility of tailoring electronic and magnetic functionalities in 2D materials by the intentional

---

[*] rwnunes@fisica.ufmg.br

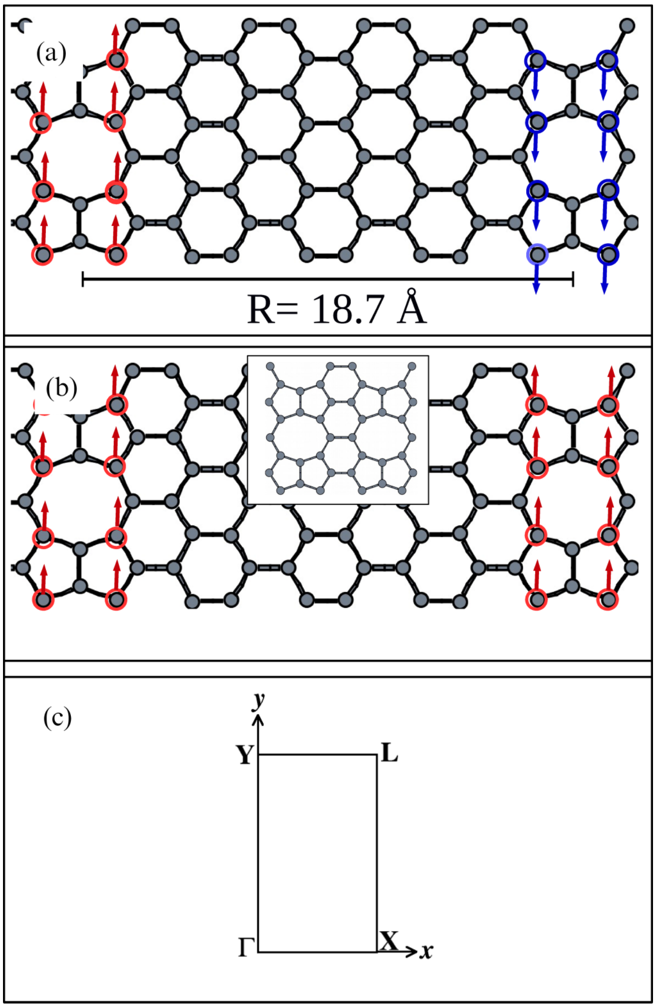

FIG. 1. Geometry of 558 linear defect cells in graphene. (a) Two periods of the 558 defect and its nearest periodic image, for the case of a defect-defect distance of $R = 18.7$ Å. Initial arrangement of atomic spins for the antiferromagentic state is indicated. (b) Initial distribution of atomic spins for the ferromagnetic state. The inset shows a 2×2 cell of the case with $R = 5.7$ Å. (c) Brillouin zone corresponding to the supercells in our study, showing special k points along symmetry lines.

application of strain. Graphene is known to withstand strains as high as 20%–25% without failure [14,29,30], being one of the 2D systems of choice for strain engineering [31]. Generally, tensile strains lead to reduced bandwidths and extended van Hove singularities, thus to enhanced exchange and correlation effects, as exemplified by the case of palladium, which displays paramagnetic states that are very close to magnetic instabilities that can be triggered by quantum confinement and strain in low-dimensional structures [32–36].

In the present study, we employ *ab initio* calculations to address the combined effects of defect-defect interaction and uniaxial or biaxial strains of up to 10% on the development of magnetic instabilities on the q1D electronic states generated by the 558 extended defect on graphene monolayers.

Our calculations indicate that conditions for the development of magnetic instabilities on the core-localized q1D 558-defect states can be tuned by uniaxial tensile strains along the defect line, and uniaxial compressive strains perpendicular to the defect line, at both limits of isolated and interacting 558 defects. A tensile strain applied along the defect line (which we refer to as a parallel tensile strain) leads to two cooperative effects that favor the emergence of itinerant magnetism in the 558-defect states, for both isolated and interacting defects: (i) enhancement of the DOS of the q1D states in the region of the Fermi level and (ii) tuning of the Fermi level to the maximum of the related DOS peak. On its turn, a compressive strain applied in the direction perpendicular to the defect line favors magnetic states by also tuning the Fermi level, but in this case enhancement of the DOS at the Fermi level only starts at defect-defect distances of the order of 20 Å, with the effect becoming more pronounced as we approach the limit of isolated (noninteracting) defects.

On the other hand, uniaxial compressive strains applied along the defect line, as well as perpendicular tensile strains, are shown to be detrimental to the development of magnetic states on the 558 defect, because in these cases the Fermi level is found to shift away from the maximum of the defect DOS. This untuning of the Fermi level inhibits the emergence of the magnetic states.

In the case of isotropic biaxial tensile strains, we find that the stabilization of a magnetic state occurs only in the limit of interacting defects, for strains of up to 5%.

The above suggests an optimum scenario for the stabilization of magnetic states in the 558 linear defect in graphene: a combination of a tensile parallel strain with a compressive perpendicular one. Indeed, for isolated (noninteracting) 558 defects submitted to biaxial strains with (parallel,perpendicular) components of (5%,−5%) and (10%,−10%) we find an increase in the values of the magnetic moments of the ferromagnetic states, compared to the respective uniaxial values. However, for 558 defects interacting at a distance $R = 10.0$ Å, a (5%,−5%) strain combination produces an increase in the magnitude of the magnetic moment, but a (10%,−10%) combination fully quenches the magnetic moment.

These results are also analyzed by considering the evolution of the DOS in each case. For the noninteracting case, the DOS at the Fermi level increases for both the (5%,−5%) and (10%,−10%) strains, and the Fermi level is tuned to the maximum of the defect peak. For the interacting case, we observe the same tendency for the (5%,−5%) biaxial strain. However, in the case of the (10%,−10%) strain we observe a splitting of the peak of defect states, with a reduction of the magnitude of the DOS with respect to the unstrained state. Furthermore, the Fermi level is tuned to the lower-energy split peak, resulting in the quenching of the magnetic state.

Our analysis in the present work does not consider buckling effects, which are important in the case of compressive strains [37,38]. Critical compressive strains for buckling in monolayer graphene have been found in the literature to depend strongly on interaction of the monolayer with the substrate, and also on the density of defects in the layer. Vacancies, for example, are found to reduce the value of critical strains, while interaction with a substrate has been shown to lead to critical buckling strains that are higher, by six orders of magnitude, than in freestanding layers [37,38]. Values of critical strains of the order of 1%–2% have been reported, which fall on the interval of compressive strains we consider. Buckling effects on the magnetic states of the 558 defect will be addressed in a forthcoming work.

Regarding the meaning of our DFT-theory mean-field results, it must be stressed that, because of their 1D nature, these correlated magnetic states do not show long range order [39]. Instead, they present algebraic correlation functions, and the magnetic states we find in our calculations should manifest themselves in experimental samples as magnetic domains with a null average macroscopic magnetization.

The paper is organized as follows: in Sec. II we describe the first-principles methodology employed in our calculations. In Sec. III we present our results, with a discussion on the energetics of the strained states of the 558 defect in Sec. III A, followed by a discussion of the effects of uniaxial and biaxial strains on the stabilization of magnetic states, with effects of parallel strains discussed in Sec. III B, of perpendicular strains in Sec. III C, and of biaxial strains in Sec. III D. In Sec. IV we summarize the conclusions of our work.

II. METHODOLOGY

In our calculations we employ the SIESTA code [40] implementation of Kohn-Sham density functional theory (DFT), within the generalized-gradient approximation (GGA) [41,42] for the exchange and correlation functional. Interactions between valence electrons and ionic cores are treated using norm-conserving pseudopotentials in the Kleinman-Bylander factorized form [43,44]. A double-zeta LCAO basis set, augmented with polarization orbitals, is used to expand the electronic wave functions. In all calculations, an equivalent real-space mesh cutoff of 250 Ry is used, and meshes of up to 64 k points along the defect direction in the Brillouin zone are used to converge the electronic density and the density of states.

Full structural relaxation of internal degrees of freedom is performed, with forces on atoms reaching values of 0.01 eV/Å or lower in all cases. For the equilibrium (unstrained) geometries, the residual pressure on the supercell is lower than 1 kbar in all cases. In a few selected cases, convergence of energies and magnetic moments is verified with calculations employing larger k-point sets and a mesh cutoff of 300 Ry, to ensure that our results are converged with respect to calculational parameters.

For the ferromagnetic and spin-unpolarized calculations, the supercells we employ contain a single 558 extended defect, and the supercell vector in the direction perpendicular to the defect line (the x axis of the cell) determines the nearest defect-defect distance R in the periodic array of defects generated by the use of periodic boundary conditions, as shown in Fig. 1. In the case of the antiferromagnetic (AFM) calculations, the supercell is doubled along the x axis and contains two 558 defects. The initial AFM spin distribution in this case is shown in Fig. 1 and described in the next section.

Supercells containing 558 defects may be classified by the number N of "buffer" zigzag chains of carbon atoms in the bulk part of the cell, as suggested in Ref. [12]. In our analysis we find it more expedient to classify the supercells by the distance R between the 558 defect in the unit cell and its closest periodic images. We consider a total of six different supercells: $R = 5.7$ Å ($N = 0$), $R = 10.0$ Å ($N = 2$), $R = 14.3$ Å ($N = 4$), $R = 18.7$ Å ($N = 6$), $R = 23.0$ Å ($N = 8$), and $R = 27.3$ Å ($N = 10$). These supercells cover the range of defect-defect distances between $R = 5.7$ Å, the smallest possible distance between adjacent 558 defects, and $R = 27.3$ Å, a value at which defect-defect interaction is negligible and the electronic properties of the defect are characteristic of isolated defects.

The geometry of the supercell with $R = 18.7$ Å, with six buffer chains between defects, is shown in Fig. 1. The inset in Fig. 1(b) shows a 2 × 2 frame of the supercell with $R = 5.7$ Å, with no buffer chains between the 558 defect in the unit cell and its closest periodic images.

III. RESULTS AND DISCUSSION

In the following discussion, the density of states (DOS) of the electronic states of graphene sheets containing 558 defects, as a function of energy, is denoted as $\mathcal{N}(\epsilon)$. The maximum of the peak introduced in the DOS by the 558-defect states, in the region of the Fermi level, is denoted as $\mathcal{N}_{\max}(\epsilon)$, and for the value of the DOS at the Fermi level we write $\mathcal{N}(\epsilon_F)$.

Our results are analyzed in terms of the Stoner criterion (SC) for itinerant magnetic instabilities:

$$I\mathcal{N}(\epsilon_F) \geqslant 1, \tag{1}$$

where I is the exchange integral and $\mathcal{N}(\epsilon_F)$ is the DOS at the Fermi level.

Our focus is to address the effects of defect-defect interaction and strain on the development of magnetic states on the q1D electronic states of the 558 defect in graphene, based on the heuristics of the SC. While the strong localization of the q1D defect states favors both factors in the left-hand side of the SC inequality, in Ref. [11] it was shown that, in the isolated-defect limit, tuning the Fermi level with n-type doping is required for the ferromagnetic instability to set in, which means that the SC is not met for an isolated 558 defect in a neutral and unstrained graphene layer.

We consider ferromagnetic (FM) and antiferromagnetic (AFM) couplings between defects [12], as well as the spin-unpolarized nonmagnetic case (NM). Figure 1 shows schematically the starting spin distribution for the initial states of the FM and AFM states in our DFT calculations. After electronic self-consistency is achieved, we obtain the corresponding FM and AFM states for the 558 defect. We have also attempted several other initial spin configurations, such as an antiferromagnetic coupling between the two zigzag chains on the core of the 558 defect (as considered in Ref. [12]), as well as other initial antiferromagnetic arrangements of initial spin states for the atoms along the core of the 558 defect. At the GGA level, these converge either to the FM or the AFM states shown in Fig. 1.

A. Energetics

We start by addressing the combined effects of defect-defect interaction and a homogeneous parallel tensile strain on the energetics and magnetic states of the 558 linear defect. Figure 2 shows the difference in total energy per defect periodic unit, with respect to the energy of the NM state, for the FM ($\Delta E_{\text{tot}}^{\text{FM}} = E_{\text{tot}}^{\text{FM}} - E_{\text{tot}}^{\text{NM}}$) and AFM states ($\Delta E_{\text{tot}}^{\text{AFM}} = E_{\text{tot}}^{\text{AFM}} - E_{\text{tot}}^{\text{NM}}$) of the 558 defect as functions of

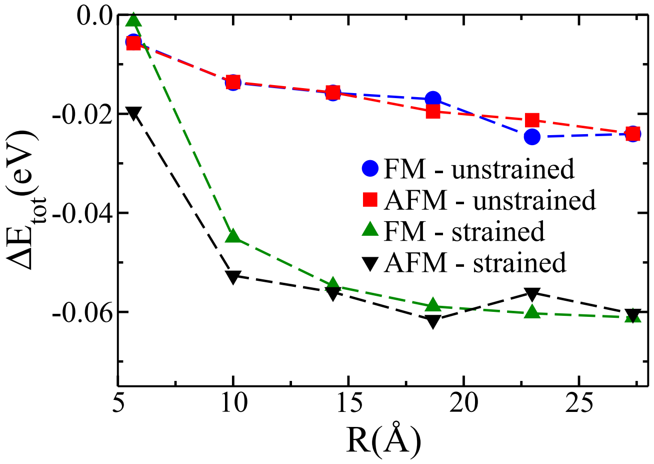

FIG. 2. Relative energies (per defect unit) of magnetic and nonmagnetic states of the 558 linear defect (see text) in graphene as functions of defect-defect distance R. Blue circles show the energy of the ferromagnetic (FM) state of the unstrained defect, relative to the nonmagnetic case, as a function of defect-defect distance. Red squares show the same for the antiferromagnetic (AFM) unstrained state. Green up triangles show energy of the FM state at a 10% uniaxial tensile strain (along the defect direction). Black down triangles show the same for the AFM state. Lines are guide to the eye.

the defect-defect distance R. The figure shows ΔE_{tot} for the equilibrium (nonstrained) as well as for the uniaxially strained cases, at a parallel strain of 10%.

Figure 2 shows that the equilibrium FM and AFM states are nearly energy degenerate for all values of R. A discernible trend is that, for both the FM and AFM states, ΔE_{tot} increases in magnitude as the defect-defect interaction is reduced with increasing R. A small energy difference of $\sim$2.5 meV (per defect periodic unit), favoring the AFM state, is observed for $R = 18.7$ Å, while for $R = 23.0$ Å the FM state is favored by $\sim$3.4 meV. At the largest distance of $R = 27.3$ Å, defect-defect interaction effects are negligible and the two phases are degenerate, with E_{tot} values that are smaller than the NM case by 24 meV per defect periodic unit.

The energetics of the magnetic states of the strained 558 defect shows a richer structure. The AFM state is favored for all values of R, except for the case of $R = 23.0$ Å, and the FM-AFM split in energy is much larger at small defect-defect separations than in the unstrained case, with the AFM state being favored by 20 meV at the smaller distance of $R = 5.7$ Å. At larger defect-defect distances, the FM and AFM states become nearly degenerated, with energies that are lower than the NM case by $\sim$55-62 meV, compared with the unstrained results of 24 meV.

Note that the difference in energy between the AFM and FM cases does not show a monotonic behavior with respect to the defect-defect distance. For $R = 14.3$ Å the two states are degenerate, and at a distance $R = 23.0$ Å there is a slight stability inversion, with the AFM state becoming more stable. In graphene, it is know that the interaction between localized moments shows antiferromagnetic coupling when the moments are localized in sites of different sublattices, and ferromagnetic coupling when localized on sites of the same sublattice. The presence of the 558 defect breaks the sublattice assignment, because this defect is the domain boundary across which the sublattice assignment is switched. We believe that there is no physical reason to expect, *a priori*, that either coupling is favored at a given distance. Generally, we obtain that a parallel uniaxial strain enhances the stability of the magnetic states with respect to the NM state.

While the energies of the FM and AFM states in Fig. 2 are given with respect to the spin-unpolarized state, for each value of R, it is worth examining the effect of strain on the energetics of the 558 defect with respect to pristine graphene. This reflects the extent to which the introduction of the 558 defect changes the elastic constants of the graphene layer. For this, we analyze the $R = 10.0$ Å case that shows the largest split between the strained FM and AFM states in Fig. 2.

The proper quantity for this comparison is the formation energy per defect unit, defined as

$$E_f^{558} = E_{\text{tot}}^{558}(N) - N\mu^{\text{bulk}}, \tag{2}$$

where $E_{\text{tot}}^{558}(N)$ is the total energy of a supercell with N atoms containing one 558 defect unit, and μ^{bulk} is the energy per atom of a pristine graphene calculation.

For the unstrained nonmagnetic state we have $E_f^{558} = 2.34$ eV. At a 10% parallel tensile strain, we obtain $E_f^{558} = 2.45$ eV for the nonmagnetic state, which shows that introduction of the 558 linear defect, even in such large concentrations as in the $R = 10.0$ Å supercells, makes the graphene slightly stiffer than a pristine layer, but the change is not significant. Note that energy differencies between the magnetic and nonmagnetic states are two orders of magnitude smaller than their formation energies with respect to pristine graphene, for both unstrained and strained layers.

B. Magnetic states: Effects of uniaxial parallel strain

1. *Parallel tensile strain*

Shifting gears now to the onset of magnetic states, we show in Fig. 3 the magnetic moment per defect unit μ (in units of the Bohr magneton, μ_B) as a function of parallel tensile strain for different values of R. For the unstrained cases (0% strain), we observe that μ decreases with increasing R, with the exception of the anomalous case of $R = 5.7$ Å, that shows a very small value of μ. Magnetic moment values at the largest defect-defect separations in our study, $\mu = 0.007\ \mu_B$ for $R = 23.0$ Å and $\mu = 0.003\ \mu_B$ for $R = 27.3$ Å, are very small for the unstrained defects. Figure 3 also shows that the rate of increase of μ with strain increases with R.

Indeed, at a 4% parallel strain the values of μ are nearly the same for all values of R (with the exception of the anomalous case of $R = 5.7$ Å that we discuss in more detail below), and for a strain of 10% the behavior of μ as a function of R is reversed, with μ becoming an increasing function of the defect-defect separation, for the range of R values we consider. Note that at the larger defect-defect distances ($R = 23.0$ Å and $R = 27.3$ Å), for strains between 1% and 2% the μ values increase by two orders of magnitude and become comparable to those for smaller values of R.

The case of $R = 5.7$ Å is anomalous, with very small values of μ for parallel tensile strains up to 5%. In this case, strains

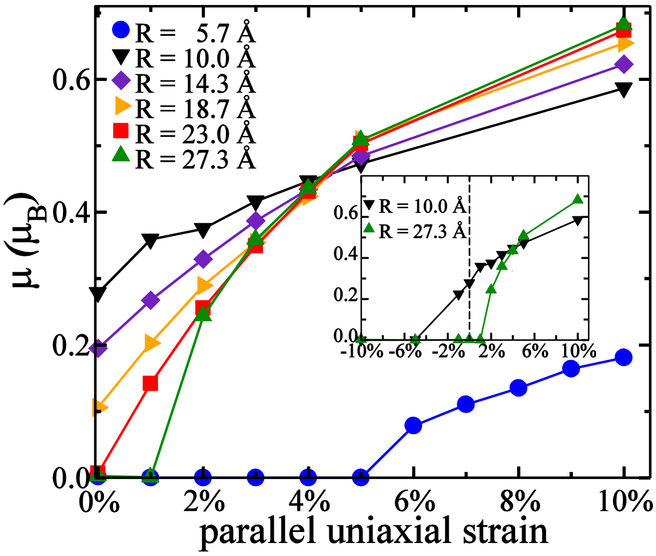

FIG. 3. Magnetic moment μ (per defect periodic unit), in units of the Bohr magneton, as a function of uniaxial parallel tensile strain (see text), for the six values of defect-defect distance R. The inset shows μ as a function of parallel strain in the range from -10% (compressive) to 10% (tensile), for $R = 10.0$ Å and $R = 27.3$ Å. Lines are guide to the eye.

larger than a threshold value between 5% and 6% are needed for μ to reach values of 0.1–0.2 μ_B.

In order to facilitate the visualization of these trends, in Fig. 4 we plot the data from Fig. 3 as a function of R for three different values of parallel tensile strain: unstrained, 4%, and 10%.

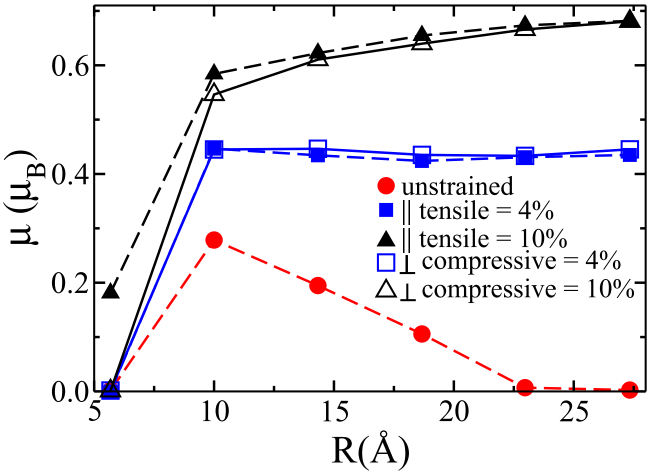

FIG. 4. Magnetic moments as a function of defect-defect distance R, for the unstrained defect (red circles), for parallel tensile strain values of 4% (blue filled squares) and 10% (black filled triangles), and for perpendicular compressive strain values of -4% (blue hollow squares) and -10% (black hollow triangles). Lines are guide to the eye.

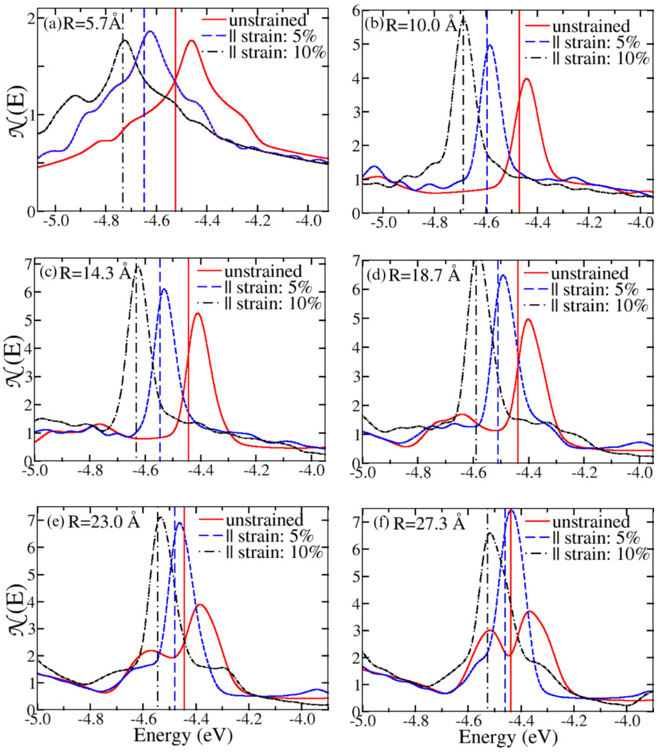

FIG. 5. Density of states $\mathcal{N}(\epsilon)$ of graphene monolayers with 558 defects under uniaxial parallel tensile strain, for the six values of R, showing results for three strain values: unstrained (red solid lines), 5% (blue dashed lines), and 10% (black dashed-dotted lines). The Fermi level is indicated by the vertical lines in each case.

Generally, from Figs. 3 and 4 we conclude that defect-defect interaction favors the emergence of itinerant magnetism in unstrained 558 defects, with the exception of the case of defects at their closest possible separation ($R = 5.7$ Å). In its turn, a parallel tensile strain also favors the onset of magnetism, and supersedes the effect of interaction, starting at about a 4% parallel strain, as shown in Fig. 4. For a 4% parallel strain, the magnetic moment per defect unit is nearly independent of R (for $R \geqslant 10.0$ Å), and for larger strains μ increases with distance, in stark contrast with the behavior of the unstrained defects.

The mechanisms behind these trends, and also behind the behavior of the anomalous case of defects at a distance of $R = 5.7$ Å, can be understood from the perspective of the Stoner criterion. Figure 5 shows the DOS, $\mathcal{N}(\epsilon)$, in the Fermi level region, for a graphene layer containing an array of 558 defects, with the defect-defect distance indicated in each subpanel. For each case, we show $\mathcal{N}(\epsilon)$ for the unstrained state, and for the cases of 5% and 10% parallel tensile strains. We recall that for a pristine graphene layer, $\mathcal{N}(\epsilon)$ vanishes at the Dirac point (the Fermi level in a neutral layer). Hence the peaks we observe in $\mathcal{N}(\epsilon)$ in Fig. 5 correspond to the resonant q1D states introduced by the 558 defect in the region of the Fermi level.

Starting from the anomalous $R = 5.7$ Å case in Fig. 5(a), we observe that under a parallel tensile strain the maximum of the defect-induced resonant peak in the DOS, $\mathcal{N}_{\max}(\epsilon)$, remains essentially unaltered. This indicates that strain does not enhance the localization of the defect states at the Fermi level, and its only effect in this case is a better tuning of the Fermi level, that shifts closer to $\mathcal{N}_{\max}(\epsilon)$ in Fig. 5(a). This explains why, at this defect-defect distance, the 558 defect only develops a magnetic moment for strains above 5%. Thus, the only factor in Eq. (1) that is affected by application of a parallel tensile strain in this case is the value of the DOS at the Fermi level $\mathcal{N}(\epsilon_F)$ and the exchange integral remains essentially unchanged.

At larger distances this picture changes, as shown in Figs. 5(b)–5(f) where we observe that a parallel tensile strain induces two effects in the electronic structure of the 558 defect. The first one is a better tuning of the Fermi level that shifts closer to $\mathcal{N}_{\max}(\epsilon)$, as in the $R = 5.7$ Å case, but we also observe an enhancement of $\mathcal{N}_{\max}(\epsilon)$ itself, due to a stronger localization of the defect states in the Fermi level region. Note that at the two largest distances in our study ($R = 23.0$ Å and $R = 27.3$ Å), the evolution of the DOS and also of the Fermi level position with strain is more complex due to the presence of two peaks of defect states in $\mathcal{N}(\epsilon)$ near the Fermi level, in the unstrained state, that merge into a single peak when strain is applied

Regarding the anomalous $R = 5.7$ Å case, we speculate that at this distance the lack of a bulk region onto which the defect states can relax (as shown in the inset in Fig. 1), inhibits the enhancement of the localization of the defect states induced by the parallel tensile strain that we observe at larger distances, where the defects are surrounded by bulk material.

The enhancement of localization, hence of the exchange integrals in Eq. (1), induced by the application of strain is a result of the changes in the 558-defect electronic states induced by strain. In Fig. 6 we show the band structures for the unstrained and 10% parallel-strained cases, for three different values of R. Figure 6(a) shows the $R = 5.7$ Å case, where extended van Hove singularities do not appear in the band structure of the unstrained defect. At this defect-defect distance, even for the 10%-strained case in Fig. 6(b), we observe no extended van Hove singularities in the band structure, and the only effect of strain is the tuning of the Fermi level, as discussed in the previous paragraph. This explains why for $R = 5.7$ Å the system develops only a moderate value of μ, even for such large value of strain, and generally the behavior of μ with strain does not follows the trends we observe at larger defect-defect distances.

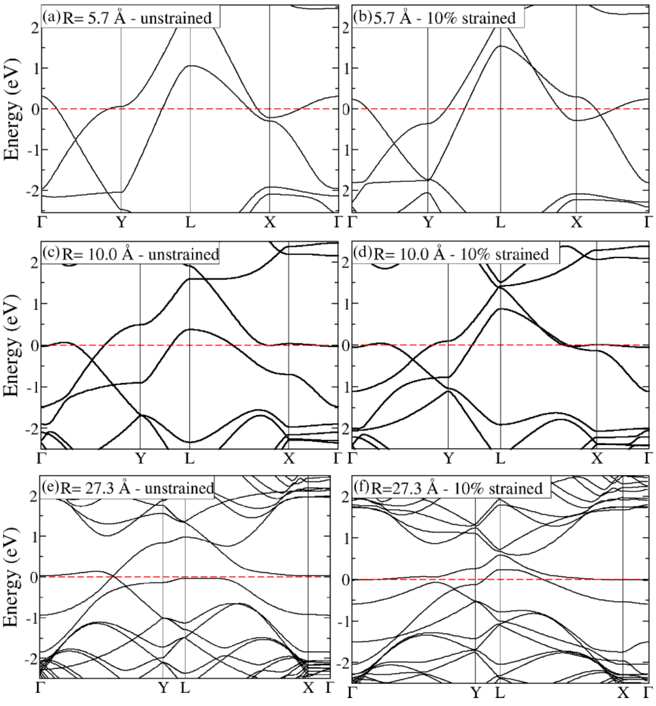

FIG. 6. Evolution of the band structure of defect states with respect to parallel tensile strain. (a) and (b) The band structures of the unstrained and 10%-strained cases, respectively, for a defect-defect distance of $R = 5.7$ Å. (c) and (d) The same for $R = 10.0$ Å. (e) and (f) The same for $R = 27.3$ Å.

When 558 defects are separated by $R = 10.0$ Å, extended van Hove singularities, in the form of large flat portions of the defects bands at the Fermi level, appear in the band structure for the unstrained defect, as shown in Fig. 6(c). This observation, along with the fact that the Fermi level in this case is very near $\mathcal{N}_{\max}(\epsilon)$, are the reasons behind the development of a large value of μ already for the unstrained defects in this case. For the strained states, a better tuning of the Fermi level to $\mathcal{N}_{\max}(\epsilon)$ [shown in Fig. 5(b)], coupled with an enhancement of the extended van Hove singularities and hence of $\mathcal{N}_{\max}(\epsilon)$ itself, explain the increase of μ with increasing strain displayed in Fig. 3. The increase in $\mathcal{N}_{\max}(\epsilon)$ is due to two factors: (i) an enlargement of the flat portions of the bands at the Fermi Level and (ii) a reduction of the bandwidths of the defect bands, shown in Fig. 6(d).

Strain plays an even more decisive role in the limit of isolated (noninteracting) defects ($R = 27.3$ Å). The unstrained defect shows a borderline behavior, with a very small value of μ. Given the presence of quite broad van Hove singularities in the band structure of the unstrained defect, as displayed in Fig. 6(e), it is to be expected that tensile strains in this case should drive the system towards a more robust magnetic state. Indeed, for a threshold parallel tensile strain between 1% and 2% the system develops a sizable value of $\mu = 0.24\ \mu_B$.

Further increase in the value of μ for larger strains is explained along the same reasoning as the $R = 10.0$ Å case, i.e., better tuning of the Fermi level to $\mathcal{N}_{\max}(\epsilon)$ and an enhancement of the flat portions of the defect bands that leads to more localized states and enhanced exchange effects. For this noninteracting case, Fig. 6(f) shows a marked increase in the width of the extended van Hove singularities lying at the Fermi level, for a 10% parallel tensile strain, along the **Γ-Y** and **L-X** lines in the Brillouin zone [both are parallel to the defect direction, as shown in Fig. 1(c)].

2. *Parallel compressive strain*

While parallel tensile strains are expected to drive the system towards the atomic limit, and hence favor a magnetic state, we expect the opposite effect from a parallel compressive strain. Indeed, as shown in the inset in Fig. 3, for the $R = 10.0$ Å and $R = 27.3$ Å cases, a parallel compressive strain inhibits the formation of a magnetic state in the 558 defect. In the $R = 10.0$ Å case, the magnetic moment drops to zero when a 5% parallel compressive strain is applied on the graphene layer.

The reason for this quenching of the magnetic is that a parallel compressive strain causes an untuning of the Fermi level that is shifted away from $\mathcal{N}_{\max}(\epsilon)$, as shown in Figs. 7(a) and 7(b) for the $R = 10.0$ Å and $R = 27.3$ Å cases,

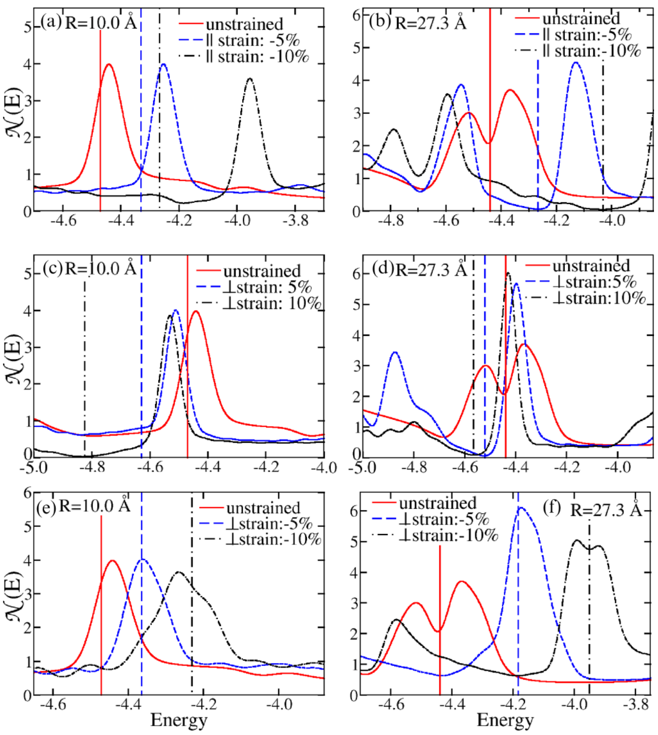

FIG. 7. (a) and (b) Density of states $\mathcal{N}(\epsilon)$ of graphene monolayers with 558 defects under uniaxial parallel compressive strain, for $R = 10.0$ Å and $R = 27.3$ Å, respectively. (c) and (d) $\mathcal{N}(\epsilon)$ of graphene monolayers with 558 defects under uniaxial perpendicular tensile strain, for $R = 10.0$ Å and $R = 27.3$ Å, respectively. (e) and (f) $\mathcal{N}(\epsilon)$ of graphene monolayers with 558 defects under uniaxial perpendicular compressive strain, for $R = 10.0$ Å and $R = 27.3$ Å, respectively. In each case results for three strain values are displayed: unstrained (red solid lines), 5% (blue dashed lines), and 10% (black dashed-dotted lines), and the Fermi level is indicated by the vertical lines.

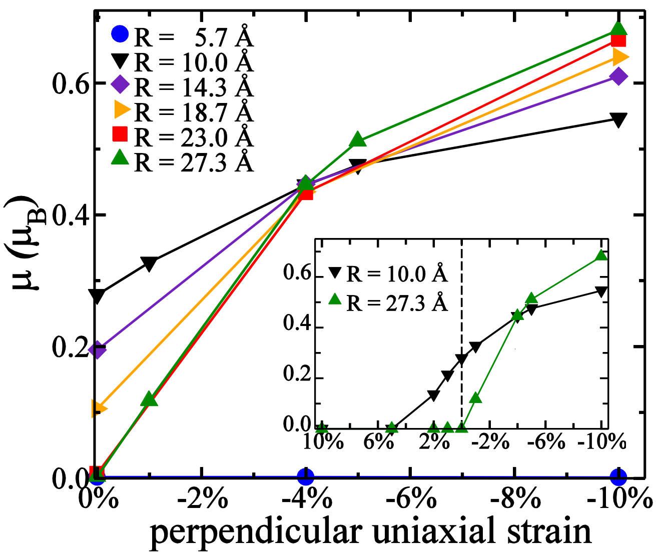

FIG. 8. Magnetic moment μ (per defect periodic unit), in units of the Bohr magneton, as a function of uniaxial perpendicular compressive strain (see text), for the six values of defect-defect distances R. The inset shows μ as a function of perpendicular strain in the range from -10% (compressive) to 10% (tensile), for $R = 10.0$ Å and $R = 27.3$ Å. Note that in both figures the strain axis is inverted, with negative (positive) values on the right (left). Lines are guide to the eye.

respectively. As a result $\mathcal{N}(\epsilon_F)$ becomes very small, and the magnetic state is inhibited, as indicated by the Stoner criterion.

One marked difference between the effects of tensile and compressive parallel strains is that in the interacting limit ($R = 10.0$ Å) a compressive strain does not cause an increase in $\mathcal{N}_{\max}(\epsilon)$, while in the noninteracting limit ($R = 27.3$ Å) $\mathcal{N}_{\max}(\epsilon)$ increases by 21%. We have also computed the DOS under a parallel compressive strain for the other values of the defect-defect distance in our study (not shown in Fig. 7), and we observe an enhancement of $\mathcal{N}_{\max}(\epsilon)$ only at the noninteracting limit.

Another telling distinction is observed in the noninteracting case, regarding the two sets of defect states that compose the double-peak structure in the DOS of the unstrained state. While the two peaks merge into a single broadened peak under a tensile strain [Fig. 5(f)], they get further separated into two distinct peaks under a compressive strain [Fig. 7(b)].

To summarize, the foregoing discussion shows that: (i) a parallel tensile strain favors the emergence of magnetic states in the 558 defect in graphene, by enhancing both factors encoded in the Stoner criterion in Eq. (1), for all defect-defect distances in our study; and (ii) a parallel compressive strain causes an untuning of the Fermi level that shifts away from $\mathcal{N}_{\max}(\epsilon)$, at both limits of interacting and noninteracting defects, and leads to an increase in $\mathcal{N}_{\max}(\epsilon)$ only at the noninteracting limit.

C. Magnetic states: Effects of perpendicular uniaxial strain

In the present section we consider the effects of perpendicular strains, analyzing in detail the strongly interacting $R = 10.0$ Å case, that displays the largest value of μ for the unstrained defects, and the noninteracting $R = 27.3$ Å case. These two examples suffice to highlight the general trends and the generality of the results will be pointed out as we proceed with the discussion.

1. *Perpendicular compressive strain*

Figure 8 shows the effect of a compressive perpendicular strain on the magnetic moment of the 558 defect, for the six defect-defect distances in our study. The trends are essentially the same as in the case of a parallel tensile strain, i.e., a compressive perpendicular strain favors the emergence of magnetic states in the 558 defect. Figure 4 confirms that the same analysis we employed for the parallel tensile strain applies here, with the effects of strain superseding the effects of interaction at a 4% perpendicular compressive strain, as indicated by the hollow symbols in Fig. 4.

An inspection of the DOS further confirms the similarity of the two cases, parallel tensile and perpendicular compressive strains, as shown by the $\mathcal{N}(\epsilon)$ curves in Figs. 7(c) and 7(d), for the $R = 10.0$ Å and $R = 27.3$ Å cases, respectively. Note that, for $R = 10.0$ Å, the effect of the perpendicular strain on $\mathcal{N}(\epsilon)$ is mainly to tune the Fermi level to $\mathcal{N}_{\max}(\epsilon)$, without an increase in the value of $\mathcal{N}_{\max}(\epsilon)$ itself, in this case. This explains why at a defect-defect distance of $R = 10.0$ Å the value of μ shows a slower increase with perpendicular compressive strain, as displayed in Fig. 8, than in the case of a parallel tensile strain in Fig. 3.

On the other hand, for $R = 27.3$ Å we observe both a tuning of the Fermi level and an enhancement of $\mathcal{N}_{\max}(\epsilon)$ under a perpendicular compressive strain, and as a result the rate of increase of μ with strain is very similar in the two strain scenarios, in this case.

2. *Perpendicular tensile strain*

Figures 7(e) and 7(f) show the evolution of $\mathcal{N}(\epsilon)$ with perpendicular tensile strain, for the $R = 10.0$ Å and $R = 27.3$ Å cases, respectively. The Fermi level shifts away from $\mathcal{N}_{\max}(\epsilon)$ in both cases, showing that the effect of a perpendicular tensile strain on the 558 defect is similar to that of a parallel compressive strain, in the sense that both lead to an untuning of the Fermi level, as seen in Figs. 7(a), 7(b) 7(e), and 7(f). As a result, under a perpendicular tensile strain, no magnetic instability is observed for the isolated defects ($R = 27.3$ Å) and a full quenching of the magnetic moment obtains for the interacting case ($R = 10.0$ Å) when the value of the applied strain reaches the value of 5%, as shown in the inset in Fig. 8.

These two strain scenarios are also similar in the sense that in the case of interacting defects in Fig. 7(e) we observe no increase in the value of $\mathcal{N}_{\max}(\epsilon)$, while for an isolated defect in Fig. 7(f) $\mathcal{N}_{\max}(\epsilon)$ increases, being almost twice as large for a 5% perpendicular strain than in the unstrained defect.

In summary, compressive and tensile perpendicular strains have opposite effects on the emergence of magnetic states in the 558 defect, with the former favoring a magnetic state by causing a tuning of the Fermi level to $\mathcal{N}_{\max}(\epsilon)$, while the latter leads to an untuning of the Fermi level and a quenching of the magnetic moments. Both compressive and tensile strains lead to an enhancement of $\mathcal{N}_{\max}(\epsilon)$ starting at a defect-defect distance of $R = 18.7$ Å, with the effect becoming more pronounced as we approach the limit of isolated (noninteracting) defects.

D. Biaxial strain

Now that we have analyzed the effects of parallel and perpendicular uniaxial strains, we conclude by addressing the effects of biaxial strains. From the foregoing discussion, we know that for an isolated 558 defect both parallel and perpendicular strains tend to enhance the extended van Hove singularities of the defect states, hence both lead to an enhancement of exchange effects. On the other hand, the effect of uniaxial strains on the value of the DOS at the Fermi level can be separated into two cases: (i) parallel tensile and perpendicular compressive strains lead to larger values of $\mathcal{N}(\epsilon_F)$ (the tuning effect in the above discussion) and (ii) parallel compressive and perpendicular tensile strains lead to a fast untuning of the Fermi level and hence to rather low values of $\mathcal{N}(\epsilon_F)$.

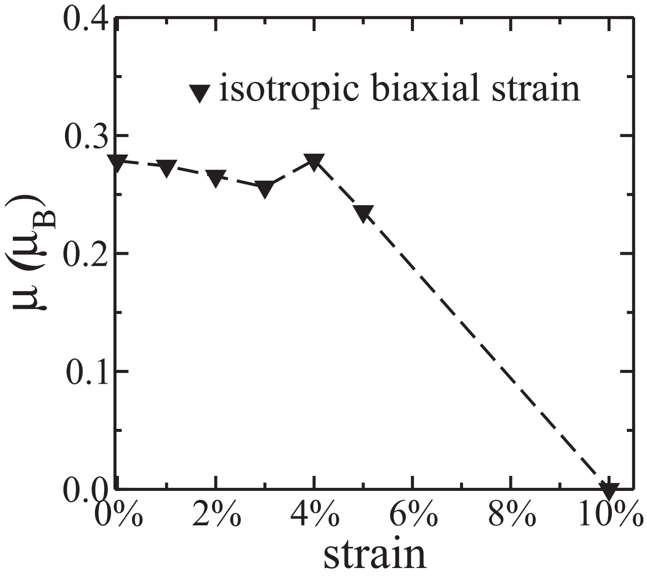

FIG. 9. Magnetic moment μ (per defect periodic unit), in units of the Bohr magneton, as a function of isotropic biaxial tensile strain, for a defect-defect distance $R = 10.0$ Å. Line is guide to the eye.

We analyze now the combined effects of parallel and perpendicular strains. We have performed calculations of isotropic biaxial tensile strains of up to 10% for all defect-defect distances in our study. We obtain a magnetic state only for the $R = 10.0$ Å case. For the other five values of R, magnetic moments were either null or negligible for all values of biaxial tensile strains from 1% to 10%.

The behavior of μ with strain for the $R = 10.0$ Å case is shown in Fig. 9. For biaxial strains of up to 5% the tuning and untuning effects of the two components of strain nearly cancel each other, and μ remains nearly constant, but a downwards trend can be observed already for strains between 4% and 5%. For a 10% tensile biaxial strain, μ vanishes, due to the Fermi-level untuning associated with the perpendicular component of strain. In Fig. 10(a) we show the evolution of the DOS with biaxial strain for this case, where the competition between the effects of the two components of strain can be observed: while $\mathcal{N}_{\max}(\epsilon)$ increases with biaxial strain, the Fermi level shifts away from $\mathcal{N}_{\max}(\epsilon)$ at a 10% biaxial strain, resulting in the quenching of μ observed in Fig. 9.

From the above discussion on the effects of uniaxial strains, we expect the most interesting case to be that of a substrate that imposes a compressive strain in the direction perpendicular to the 558 line defect, and a tensile strain in the parallel direction. We have computed the cases of unisotropic biaxial strain with $(\parallel, \perp) = (5\%, -5\%)$ and $(10\%, -10\%)$ components, for the $R = 10.0$ Å and $R = 27.3$ Å cases.

We observe an overall tendency of enhancement of magnetic moments, given that we have combined the strains that favor the magnetic states in both directions. For the isolated defect, with strains of $(5\%, -5\%)$ we obtain $\mu = 0.68\ \mu_B$, from a value of $\mu = 0.51\ \mu_B$ under either case of uniaxial strain of this magnitude, and for strains of $(10\%, -10\%)$ we obtain an increase to $\mu = 0.76\ \mu_B$ from $\mu = 0.68\ \mu_B$ under uniaxial strains. However, for the interacting $R = 10.0$ Å case, while the $(5\%, -5\%)$ strain combination produces an increased $\mu = 0.56\ \mu_B$ (from uniaxial values of $\mu = 0.47\ \mu_B$),

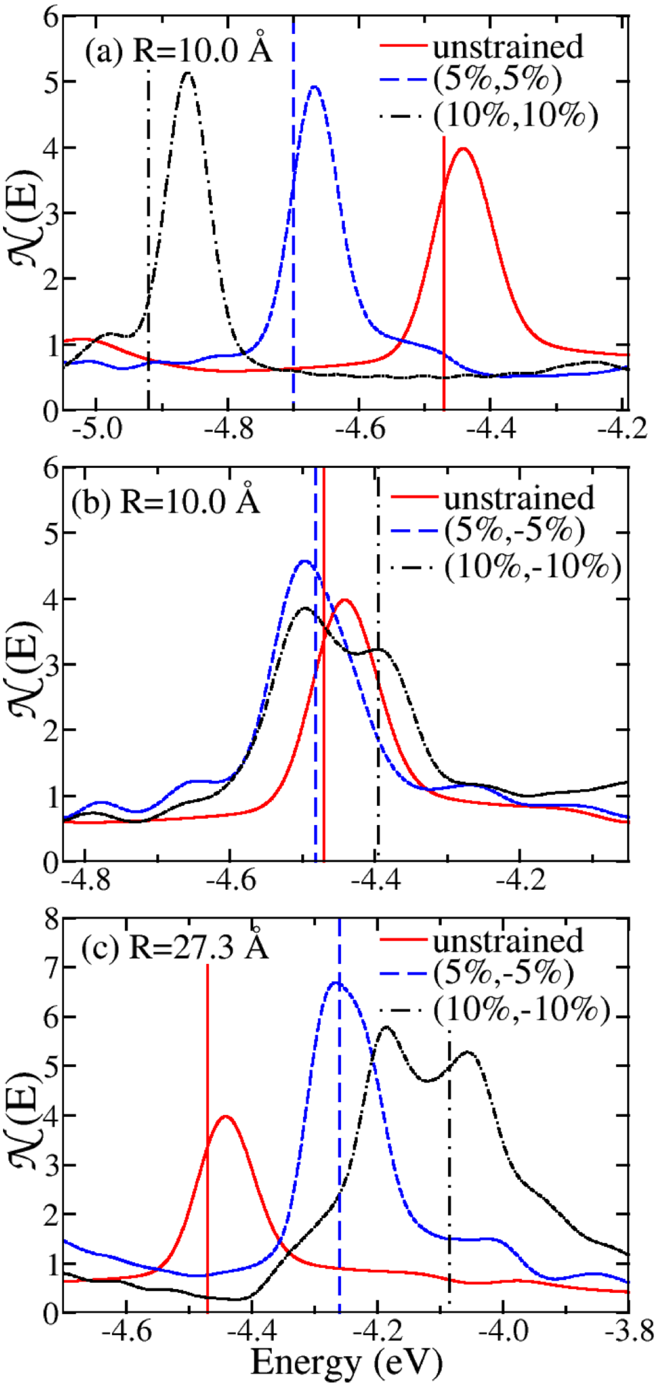

FIG. 10. (a) Density of states $\mathcal{N}(\epsilon)$ of a graphene monolayer with 558 defects under isotropic biaxial tensile strain, for $R = 10.0$ Å. (b) $\mathcal{N}(\epsilon)$ of a graphene monolayer with 558 defects under unisotropic biaxial strain, with a tensile parallel component and a compressive perpendicular component, for $R = 10.0$ Å. (c) $\mathcal{N}(\epsilon)$ of a graphene monolayer with 558 defects under unisotropic biaxial strain, with a tensile parallel component and a compressive perpendicular component, for $R = 27.3$ Å. In each case results for three strain values are displayed: unstrained (red solid lines), 5% or (5%,−5%) (blue dashed lines), and 10% or (10%,−10%) (black dashed-dotted lines), and the Fermi level is indicated by the vertical lines.

the (10%,−10%) combination fully quenches the magnetic moment.

Again, these results can be understood by looking at the evolution of the DOS in each case, as shown in Figs. 10(b) and 10(c). For the noninteracting case, $\mathcal{N}_{\max}(\epsilon)$ increases markedly for both the (5%,−5%) and (10%,−10%) strains, and the Fermi level is tuned to $\mathcal{N}_{\max}(\epsilon)$. For the interacting case, we observe the same tendency for the (5%,−5%) biaxial strain. However, in the case of the (10%,−10%) strain we observe a splitting of the peak of defect states, with a reduction of $\mathcal{N}_{\max}(\epsilon)$, with respect to the unstrained state. Furthermore, the Fermi level is tuned to the lower-energy split peak, resulting in the quenching of the magnetic state.

IV. CONCLUSIONS

In this work we have addressed the combined effects of defect-defect interaction and uniaxial or biaxial strains of up to 10% on the development of magnetic instabilities in the quasi-one-dimensional (q1D) electronic states generated by the 558 extended defect in graphene monolayers, by means of *ab initio* calculations.

We have considered uniaxial strains along the defect direction (parallel strain) and along the perpendicular direction (perpendicular strain), and isotropic and unisotropic biaxial strains. We frame our results on the basis of the Stoner criterion for itinerant magnetism, and analyze the effects of the various strain states on the basis of their impact on the two ingredients encoded in the Stoner criterion: localization of the defect-generated electronic states in the region of the Fermi level and the magnitude of the DOS of the defect states at the Fermi level.

We obtain that conditions for the development of magnetic instabilities in the 558-defect states can be tuned by either parallel tensile or perpendicular compressive strains, at both limits of isolated and interacting 558 defects. Parallel tensile strains are shown to lead to two cooperative effects that favor the emergence of itinerant magnetism in the 558-defect states: enhancement of the extended van Hove singularities of the defect states in the region of the Fermi level and tuning of the Fermi level to the maximum of the related DOS peak. Perpendicular compressive strains are also found to tune the Fermi level but, in this case, enhancement of the extended van Hove singularities is only observed at large defect-defect distances, becoming more pronounced at the limit of isolated defects.

On the other hand, parallel compressive and perpendicular tensile strains are also shown to effect an enhancement of the DOS of the defect states only in the isolated-defect limit. However, for all defect-defect distances we consider, in these two strain scenarios the Fermi level is found to shift away from the maximum of the DOS of defect states, which inhibits the emergence of the magnetic states.

In the case of isotropic biaxial tensile strains, we find that the stabilization of a magnetic state occurs only in the limit of interacting defects, for strains of up to 5%, with magnetic moments being quenched for larger values of isotropic biaxial tensile strains.

The preceding analysis indicates that a substrate that imposes a compressive strain in the direction perpendicular to the defect line, and a tensile strain in the parallel direction, would be ideal for the stabilization of magnetic states in the 558 linear defect in graphene.

Our results are relevant in the context of one-dimensional charge and spin transport in graphene layers. For example, recent work by Phillips and Mele [45] has considered the possibility that grain boundaries (including the 558 domain boundary we consider in this work) could short circuit the zero-mode Hall edge states in graphene layers with an applied transverse magnetic field. Given that a transverse magnetic field is bound to increase the magnetic moments of the 558 defect, our results reveal the possibility of spin filtering of edge states in such layers, since only one spin channel will be short circuited by a 558 defect in a ferromagnetic state.

ACKNOWLEDGMENTS

We acknowledge support from Brazilian agencies CNPq, FAPEMIG, Rede de Pesquisa em Nanotubos de Carbono, INCT de Nanomateriais de Carbono, and Instituto do Milênio em Nanotecnologia-MCT.

[1] A. H. Castro Neto, F. Guinea, N. M. R. Peres, K. S. Novoselov, and A. K. Geim, Rev. Mod. Phys. **81**, 109 (2009), and references therein.
[2] A. K. Geim and K. S. Novoselov, Nat. Mater. **6**, 183 (2007).
[3] M. I. Katsnelson, K. S. Novoselov, and A. K. Geim, Nat. Phys. **2**, 620 (2006).
[4] M. Sepioni, R. R. Nair, S. Rablen, J. Narayanan, F. Tuna, R. Winpenny, A. K. Geim, and I. V. Grigorieva, Phys. Rev. Lett. **105**, 207205 (2010).
[5] Y. Wang, Y. Huang, Y. Song, X. Zhang, Y. Ma, J. Liang, and Y. Chen, Nano Lett. **9**, 220 (2009).
[6] O. V. Yazyev and L. Helm, Phys. Rev. B **75**, 125408 (2007).
[7] E. J. G. Santos, A. Ayuela, and D. Sánchez-Portal, New J. Phys. **14**, 043022 (2012).
[8] P. O. Lehtinen, A. S. Foster, Y. Ma, A. V. Krasheninnikov, and R. M. Nieminen, Phys. Rev. Lett. **93**, 187202 (2004).
[9] E. H. Lieb, Phys. Rev. Lett. **62**, 1201 (1989).
[10] J. Kotakoski, A. V. Krasheninnikov, U. Kaiser, and J. C. Meyer, Phys. Rev. Lett. **106**, 105505 (2011).
[11] S. S. Alexandre, A. D. Lúcio, A. H. Castro Neto, and R. W. Nunes, Nano Lett. **12**, 5097 (2012).
[12] J.-C. Ren, Z. Ding, R.-Q. Zhang, and M. A. Van Hove, Phys. Rev. B **91**, 045425 (2015).
[13] J. Lahiri, Y. Lin, P. Bozkurt, I. I. Pleynik, and M. Batzill, Nat. Nanotechnol. **5**, 326 (2010).
[14] J. da Silva-Araújo, H. Chacham, and R. W. Nunes, Phys. Rev. B **81**, 193405 (2010).
[15] A. Cortijo and M. A. H. Vozmediano, Nucl. Phys. B **763**, 293 (2007).
[16] D. Gunlycke and C. T. White, Phys. Rev. Lett. **106**, 136806 (2011).
[17] J. da Silva-Araújo and R. W. Nunes, Phys. Rev. B **81**, 073408 (2010).
[18] O. V. Yazyev and S. G. Louie, Nat. Mater. **9**, 806 (2010).
[19] O. V. Yazyev and S. G. Louie, Phys. Rev. B **81**, 195420 (2010).
[20] A. W. Tsen, L. Brown, M. P. Levendorf, F. Ghahari, P. Y. Huang, R. W. Havener, C. S. Ruiz-Vargas, D. A. Muller, P. Kim, and J. Park, Science **336**, 1143 (2012).
[21] Q. K. Yu, L. A. Jauregui, W. Wu, R. Colby, J. F. Tian, Z. H. Su, H. L. Cao, Z. H. Liu, D. Pandey, D. G. Wei, T. F. Chung, P. Peng, N. P. Guisinger, E. A. Stach, J. M. Bao, S. S. Pei, and Y. P. Chen, Nat. Mater. **10**, 443 (2011).
[22] P. Simonis, C. Goffaux, P. A. Thiry, L. P. Biro, P. Lambin, and V. Meunier, Surf. Sci. **511**, 319 (2002).
[23] J. Cervenka and C. F. J. Flipse, Phys. Rev. B **79**, 195429 (2009).
[24] K. Kim, Z. Lee, W. Regan, C. Kisielowski, M. F. Crommie, and A. Zettl, ACS Nano **5**, 2142 (2011).
[25] P. Y. Huang, C. S. Ruiz-Vargas, A. M. van der Zande, W. S. Whitney, M. P. Levendorf, J. W. Kevek, S. Garg, J. S. Alden, C. J. Hustedt, Y. Zhu, J. Park, P. L. McEuen, and D. A. Muller, Nature (London) **469**, 389 (2011).
[26] J.-H. Chen, G. Autès, N. Alem, F. Gargiulo, A. Gautam, M. Linck, C. Kisielowski, O. V. Yazyev, S. G. Louie, and A. Zettl, Phys. Rev. B **89**, 121407(R) (2014).
[27] E. C. Stoner, Proc. R. Soc. London Ser. A **165**, 372 (1938).
[28] E. C. Stoner, Proc. R. Soc. London Ser. A **169**, 339 (1939).
[29] C. Lee, X. Wei, J. W. Kysar, and J. Hone, Science **321**, 385 (2008).
[30] E. Cadelano, P. L. Palla, S. Giordano, and L. Colombo, Phys. Rev. Lett. **102**, 235502 (2009).
[31] V. M. Pereira and A. H. Castro Neto, Phys. Rev. Lett. **103**, 046801 (2009).
[32] V. L. Moruzzi and P. M. Marcus, Phys. Rev. B **39**, 471 (1989).
[33] A. Delin, E. Tosatti, and R. Weht, Phys. Rev. Lett. **92**, 057201 (2004).
[34] S. S. Alexandre, J. M. Soler, P. J. S. Miguel, R. W. Nunes, F. Yndurain, J. Gomez-Herrero, and F. Zamora, Appl. Phys. Lett. **90**, 193107 (2007).
[35] S. S. Alexandre, M. Mattesini, J. M. Soler, and F. Yndurain, Phys. Rev. Lett. **96**, 079701 (2006).
[36] S. S. Alexandre, E. Anglada, J. M. Soler, and F. Yndurain, Phys. Rev. B **74**, 054405 (2006).
[37] O. Frank, G. Tsoukleri, J. Parthenios, K. Papagelis, I. Riaz, R. Jalil, K. S. Novoselov, and C. Galiotis, ACS Nano **4**, 3131 (2010).
[38] K. Yang, Y. Chen, F. Pan, S. Wang, Y. Ma, and Q. Liu, Materials **9**, ma9010032 (2016).
[39] N. D. Mermin and H. Wagner, Phys. Rev. Lett. **17**, 1133 (1966).
[40] J. M. Soler, E. Artacho, J. D. Gale, A. Garcia, J. Junquera, P. Ordejon, and D. Sánchez-Portal, J. Phys.: Condens. Matter **14**, 2745 (2002).
[41] W. Kohn and L. J. Sham, Phys. Rev. **140**, A1133 (1965).
[42] J. P. Perdew, K. Burke, and M. Ernzerhof, Phys. Rev. Lett. **77**, 3865 (1996).
[43] N. Troullier and J. L. Martins, Phys. Rev. B **43**, 1993 (1991).
[44] L. Kleinman and D. M. Bylander, Phys. Rev. Lett. **48**, 1425 (1982).
[45] M. Phillips and E. J. Mele, Phys. Rev. B **96**, 041403(R) (2017).